This article was downloaded by: [Pennsylvania State University]
On: 19 July 2013, At: 12:08
Publisher: Taylor & Francis
Informa Ltd Registered in England and Wales Registered Number: 1072954 Registered office: Mortimer House, 37-41 Mortimer Street, London W1T 3JH, UK

Philosophical Magazine
Publication details, including instructions for authors and subscription information:
http://www.tandfonline.com/loi/tphm20

A phase-field model for elastically anisotropic polycrystalline binary solid solutions

Tae Wook Heo [a], Saswata Bhattacharyya [a] & Long-Qing Chen [a]
[a] Department of Materials Science and Engineering, The Pennsylvania State University, University Park, PA 16802, USA
Published online: 19 Nov 2012.

To cite this article: Tae Wook Heo, Saswata Bhattacharyya & Long-Qing Chen (2013) A phase-field model for elastically anisotropic polycrystalline binary solid solutions, Philosophical Magazine, 93:13, 1468-1489, DOI: 10.1080/14786435.2012.744880

To link to this article: http://dx.doi.org/10.1080/14786435.2012.744880

PLEASE SCROLL DOWN FOR ARTICLE

Taylor & Francis makes every effort to ensure the accuracy of all the information (the "Content") contained in the publications on our platform. However, Taylor & Francis, our agents, and our licensors make no representations or warranties whatsoever as to the accuracy, completeness, or suitability for any purpose of the Content. Any opinions and views expressed in this publication are the opinions and views of the authors, and are not the views of or endorsed by Taylor & Francis. The accuracy of the Content should not be relied upon and should be independently verified with primary sources of information. Taylor and Francis shall not be liable for any losses, actions, claims, proceedings, demands, costs, expenses, damages, and other liabilities whatsoever or howsoever caused arising directly or indirectly in connection with, in relation to or arising out of the use of the Content.

This article may be used for research, teaching, and private study purposes. Any substantial or systematic reproduction, redistribution, reselling, loan, sub-licensing, systematic supply, or distribution in any form to anyone is expressly forbidden. Terms & Conditions of access and use can be found at http://www.tandfonline.com/page/terms-and-conditions

Philosophical Magazine, 2013
Vol. 93, No. 13, 1468–1489, http://dx.doi.org/10.1080/14786435.2012.744880

Taylor & Francis
Taylor & Francis Group

A phase-field model for elastically anisotropic polycrystalline binary solid solutions

Tae Wook Heo*, Saswata Bhattacharyya† and Long-Qing Chen

Department of Materials Science and Engineering, The Pennsylvania State University, University Park, PA 16802, USA

(*Received 30 April 2012; final version received 23 October 2012*)

A phase-field model for modeling the diffusional processes in an elastically anisotropic polycrystalline binary solid solution is described. The elastic interactions due to coherency elastic strain are incorporated by solving the mechanical equilibrium equation using an iterative-perturbation scheme taking into account elastic modulus inhomogeneity stemming from different grain orientations. We studied the precipitate interactions among precipitates across a grain boundary and grain boundary segregation–precipitate interactions. It was shown that the local pressure field from one coherent precipitate influences the shape of precipitates in other grains. The local pressure distribution due to primary coherent precipitates near the grain boundary leads to inhomogeneous solute distribution along the grain boundary, resulting in non-uniform distribution of secondary nuclei at the grain boundary.

Keywords: elasticity; polycrystalline; solid solutions; diffusion; phase-field model

Downloaded by [Pennsylvania State University] at 12:08 19 July 2013

1. Introduction

Phase transformations of solid solutions involve a complicated coupling among a number of different diffusional processes such as solute segregation/depletion, precipitate nucleation, growth, and coarsening. The thermodynamics and kinetics of these processes are often influenced by the elastic interactions in a microstructure [1]. Common internal defects such as dislocations, grain boundaries, and coherent inclusions are sources of elastic stresses in the solid solutions. For example, for systems with coherent precipitates, elastic stresses arise naturally due to the lattice parameter mismatch between the precipitate and the matrix [2–5]. Since most materials in engineering applications are polycrystalline solid solutions, computational approach for predicting phase transformations in polycrystals would be useful

*Corresponding author. Email: tuh134@psu.edu
† Current address: Materials Modeling Division, GE India Technology Center, Bangalore 560066, India.

© 2013 Taylor & Francis

Downloaded by [Pennsylvania State University] at 12:08 19 July 2013

for designing microstructures of engineering materials. However, computational modeling of diffusional processes in a polycrystalline solid solution is more challenging than those in a uniform single crystal. There are two main challenges. First, the solute-grain boundary interactions should be considered. The presence of grain boundaries leads to solute segregation or depletion due to chemical and/or elastic interaction between solute atoms and defects. To describe the solute-grain boundary interactions, several phase-field models have been proposed. Fan et al. employed the phenomenological model to induce the grain boundary segregation [6]. Cha et al. described the grain boundary as a distinguishable phase and incorporated the segregation potential within the grain boundary regime [7]. More recently, a phase-field model was proposed by Grönhagen and Ågren for modeling grain boundary segregation as well as solute drag effects [8]. The model has been successfully applied to propose the abnormal grain growth mechanism [9], simulate the solute-moving grain boundary in the strongly segregating system [10], and model the strain energy effects on grain boundary segregation and solute drag effects [11]. The second challenge is the elastic inhomogeneity of a polycrystalline solid solution. A number of approaches have been proposed to model and compute the inhomogeneous elasticity in polycrystals. Wang et al. developed a method based on the calculation of equivalent eigenstrain [12]. Tonks et al. employed a phase-field model to investigate the grain boundary motion taking into account the inhomogeneous elasticity in a bicrystal [13] where the elastic solution was computed by the numerical technique in [12]. Kim et al. incorporated elastic inhomogeneity to a phase-field grain growth model and studied grain growth behavior and texture evolution under an external load [14,15]. We recently extended an iterative-perturbation technique using the Fourier spectral method [16,17] to model the effects of elastic inhomogeneity in polycrystals [18,19].

Phase transformations and microstructure evolution in polycrystals have previously been modeled using the phase-field approach [20–25]. For example, Jin et al. [26], Artemev et al. [27] and Wang et al. [28] investigated the formation and switching of martensitic transformations in polycrystals. Choudhury et al. analyzed the evolution of ferroelectric domains in polycrystalline oxides [29,30]. The existing works mainly focused on the structural transformation and assumed the homogeneous isotropic elastic properties. However, the diffusional processes in elastically anisotropic polycrystalline solid solutions have not been extensively studied using phase-field simulations even though there have been many efforts in phase-field modeling of precipitate reactions in single crystalline solid solutions, e.g. Ni alloys [31–33], Al alloys [34–36], etc., and a few phase-field simulations of grain boundary effects on spinodal decomposition without consideration of elastic properties [37,38].

The main objective of the present work is to extend and generalize the phase-field models in [11,39] for describing the diffusional processes in elastically inhomogeneous polycrystalline solid solutions. We integrate the elasticity model for an elastically inhomogeneous polycrystalline system with phase-field equations describing diffusional processes. A binary solid solution is considered for simplicity. The elastic interactions associated with segregation and precipitations near grain boundaries are discussed.

2. Phase-field model

Diffusional processes in a polycrystalline solid solution involve interactions between inhomogeneous distribution of solute composition and grain structures. Thus, two types of field variables are required to describe the thermodynamics and kinetic processes of a polycrystalline binary solid solution. One is a conserved field variable $X(\vec{r})$ for the composition of solute, and the other is a non-conserved field variable $\eta_g(\vec{r})$ for the crystallographic orientation of grains. In the diffuse-interface description [40], the total free energy F of an inhomogeneous system is described by a volume integral as a functional of a set of continuous field variables. We adopted and extended a phase-field model of Grönhagen and Ågren [8] which is validated to be quantitatively correct by Kim and Park [9] for describing the solute–grain boundary interactions. We incorporated the elastic strain interactions of solute atoms in the presence of grain boundaries in an anisotropic binary solid solution. The functional form of the total free energy F of the solid solution is given by the following volume integral [20]:

$$F = \int_V \left\{ f_{\text{inc}} + \omega g(\eta_1, \eta_2, \ldots, \eta_g) + \frac{\kappa_c}{2}(\nabla X)^2 + \frac{\kappa_o}{2}\sum_g (\nabla \eta_g)^2 + e_{\text{coh}} \right\} \mathrm{d}V, \qquad (1)$$

where f_{inc} is the incoherent local free energy density of a solid solution, g is a multi-well free energy density function describing the grain structure, ω is the potential height of g, κ_c and κ_o are gradient energy coefficients of composition $X(\vec{r})$ and grain order parameters $\eta_g(\vec{r})$, respectively, and e_{coh} is the local coherency elastic strain energy density arising from a compositional inhomogeneity.

2.1. *Thermodynamic energy model*

The incoherent local free energy contains both the chemical and the elastic strain energy of a homogeneous solid solution. In order to explore the origin of both contributions and develop the incoherent free energy density in the presence of grain boundaries, let us start with the Gibbs free energy of a solid solution. The free energy density of the solid solution is represented by the linear combination of the chemical potentials, i.e. the partial molar Gibbs free energy, of all the species. In the case of a binary solid solution, the free energy density is given by

$$f_{\text{inc}} = \mu X + \mu_h (1 - X), \qquad (2)$$

where μ is the chemical potential of solutes and μ_h is the chemical potential of host atoms in the solid solution. To explain the free energy density of the binary system, a regular solution model is considered as the following function:

$$f_{\text{inc}} = \left[\mu^{\text{o}} + RT\ln X + \Omega(1 - X)^2\right]X + \left[\mu_h^{\text{o}} + RT\ln(1 - X) + \Omega X^2\right](1 - X), \qquad (3)$$

where μ^{o} is the chemical potential of solute atoms at standard state, μ_h^{o} is the chemical potential of host atoms at standard state, R is the gas constant, T is the temperature, and Ω is the regular solution parameter for representing the interactions among atoms. Following Cahn [41], the interaction potential E is

Downloaded by [Pennsylvania State University] at 12:08 19 July 2013

additionally incorporated to represent pure chemical interaction between a grain boundary and solute atoms, and Equation (3) becomes

$$f_{\text{inc}} = \left[\mu^{\circ} + RT\ln X + \Omega(1-X)^2 + E\right]X + \left[\mu_h^{\circ} + RT\ln(1-X) + \Omega X^2\right](1-X). \quad (4)$$

In the present model, we specify the pure chemical interaction potential E between grain boundary and solutes as $[-m\omega g(\eta_1, \eta_2, \ldots, \eta_g)]$ where m is a parameter determining the interaction strength between solute atoms and a grain boundary. Plugging the interaction potential in Equation (4) and rearranging the equation, we have the incoherent free energy density in the presence of grain boundaries as the following:

$$f_{\text{inc}} = \mu^{\circ}X + \mu_h^{\circ}(1-X) + RT[X\ln X + (1-X)\ln(1-X)] - m\omega gX + \Omega X(1-X). \quad (5)$$

Generally, the regular solution parameter contains all the contributions associated with the non-ideality of the solid solution. Ignoring all other contributions, let us focus on pure chemical and elastic interactions due to the atomic size difference (or size mismatch) between solute atoms and host atoms. Hence, the elastic strain contribution can be separated from the regular solution parameter ($\Omega = \Omega_{\text{chem}} + \Omega_{\text{elast}}^{\text{hom}}$). The elastic strain energy density (e_{hom}) of a homogeneous solid solution with composition X [2] is given by:

$$e_{\text{hom}} = \frac{1}{2}\left[C_{ijkl}\varepsilon_{ij}^m\varepsilon_{kl}^m - \langle L(\vec{n})\rangle_{\vec{n}}\right]X(1-X), \quad (6)$$

where C_{ijkl} is the elastic modulus, ε_{ij}^m is the misfit strain tensor, and $\langle L(\vec{n})\rangle_{\vec{n}}$ is the average of $L(\vec{n})$ over all the directions of $\vec{n}$ with $L(\vec{n}) = n_i\sigma_{ij}^0\Omega_{jk}\sigma_{kl}^0 n_l$, $\sigma_{ij}^0 = C_{ijkl}\varepsilon_{kl}^m$, $\Omega_{jk}^{-1} = C_{jilk}n_i n_l$, and n_i is the unit wave vector in Fourier space. The details of calculation of $\langle L(\vec{n})\rangle_{\vec{n}}$ are shown in the Appendix. Therefore, the incoherent free energy density is represented by the following expression as discussed in [11]:

$$\begin{aligned} f_{\text{inc}} = {} & \mu^{\circ}X + \mu_h^{\circ}(1-X) + RT[X\ln X + (1-X)\ln(1-X)] - m\omega gX \\ & + \Omega_{\text{chem}}X(1-X) + \frac{1}{2}\left[C_{ijkl}\varepsilon_{ij}^m\varepsilon_{kl}^m - \langle L(\vec{n})\rangle_{\vec{n}}\right]X(1-X), \end{aligned} \quad (7)$$

where Ω_{chem} is the regular solution parameter associated with the pure chemical contribution, i.e. regular solution parameter of a hypothetical solid solution in which all the atoms have the same size (This representation is similar to Cahn's in [42]). The incoherent free energy is expressed by the summation of purely chemical part and elastic strain energy of a homogeneous solid solution itself:

$$f_{\text{inc}} = [f_{\text{chem}} - m\omega gX] + e_{\text{hom}}, \quad (8)$$

where $f_{\text{chem}} = \mu^{\circ}X + \mu_h^{\circ}(1-X) + RT[X\ln X + (1-X)\ln(1-X)] + \Omega_{\text{chem}}X(1-X)$. Our total free energy without e_{hom} and the excess energy term ($\Omega_{\text{chem}}X(1-X)$) is identical to the model of Grönhagen and Ågren [8].

With regard to the misfit strain tensor ε_{ij}^m near a grain boundary, the elastic strain is relaxed when a solute atom approaches to a grain boundary due to its relatively disordered structure. Therefore, we model the strain relaxation by employing the position (or grain structure)-dependent mismatch as the following:

$$\varepsilon_{ij}^m(\vec{r}) = \varepsilon_{ij}^{m,b}\varphi(\vec{r}), \quad (9)$$

Downloaded by [Pennsylvania State University] at 12:08 19 July 2013

where $\varphi(\vec{r})$ is an interpolation function which is 1 inside grains and 0 at the center of a grain boundary and its explicit form is

$$\varphi(\vec{r}) = -\left(\frac{\phi - \phi_{\min}}{\phi_{\max} - \phi_{\min}}\right)^2 + 2\left(\frac{\phi - \phi_{\min}}{\phi_{\max} - \phi_{\min}}\right) \tag{10}$$

where $\phi = \sum_g \eta_g^2$, $\phi_{\max}$ is the maximum value of ϕ which corresponds to the value inside the bulk, and $\phi_{\min}$ is the minimum value of φ which corresponds to the value at the center of a grain boundary. $\varepsilon_{ij}^{m,b}$ is the misfit strain tensor inside the bulk. We assume dilatational strain tensor $\varepsilon_c\delta_{ij}$ for $\varepsilon_{ij}^{m,b}$ where δ_{ij} is the Kronecker-delta function, ε_c is the composition expansion coefficient of lattice parameter defined as $\frac{1}{a_0}(\frac{da}{dX})$, and a_0 is the lattice parameter of the reference homogeneous solid solution of overall composition X_0. The strain is assumed to be fully relaxed when the solute atom comes to the center of the grain boundary. Taking into account the position-dependent mismatch, we rewrite e_{hom} using Equation (9),

$$e_{\text{hom}} = \frac{1}{2}\left[C_{ijkl}\varepsilon_{ij}^{m,b}\varepsilon_{kl}^{m,b} - \langle L^b(\vec{n})\rangle_{\vec{n}}\right]\varphi(\vec{r})^2 X(1-X), \tag{11}$$

where $\langle L^b(\vec{n})\rangle_{\vec{n}}$ is the average of $L^b(\vec{n})$ over all the directions of $\vec{n}$ with $L^b(\vec{n}) = n_i\sigma_{ij}^{0,b}\Omega_{jk}\sigma_{kl}^{0,b}n_l$, $\sigma_{ij}^{0,b} = C_{ijkl}\varepsilon_{kl}^{m,b}$, $\Omega_{jk}^{-1} = C_{jilk}n_in_l$, and n_i is the unit wave vector in Fourier space. It should be noted that the prefactor $\frac{1}{2}[C_{ijkl}\varepsilon_{ij}^{m,b}\varepsilon_{kl}^{m,b} - \langle L^b(\vec{n})\rangle_{\vec{n}}]$ in Equation (11) includes the elastic properties of a grain interior only, and the interpolation function $\varphi(\vec{r})$ is responsible for the relatively disordered grain boundary structure resulting in the misfit strain relaxation near a generic grain boundary in our model. The possible variations of elastic modulus or crystallographic symmetry within the grain boundary arising from the relatively disordered grain boundary structure were not addressed in the model. One remarkable thing is that the prefactor is independent of grain orientation even if each grain has anisotropic elastic modulus. Since $\varepsilon_{ij}^{m,b}$ is a dilatational tensor, the first term $C_{ijkl}\varepsilon_{ij}^{m,b}\varepsilon_{kl}^{m,b}$ in the bracket is invariant with

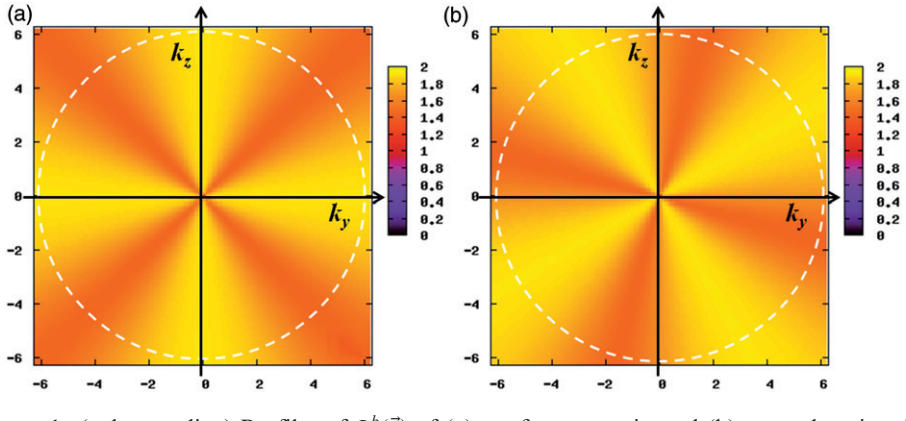

Figure 1. (colour online) Profiles of $L^b(\vec{n})$ of (a) a reference grain and (b) rotated grain with respect to the reference grain in k_y–k_z planes.

Downloaded by [Pennsylvania State University] at 12:08 19 July 2013

Downloaded by [Pennsylvania State University] at 12:08 19 July 2013

grain rotation. In addition, the second term $\langle L^b(\vec{n})\rangle_{\vec{n}}$ is a scalar quantity where all directions are equally considered. Figure 1 shows an example of the $L^b(\vec{n})$ profiles in k-space for grains of different crystallographic orientations. If we average $L^b(\vec{n})$ over all the directions, the values are the same since the profiles are just mutually rotated. Therefore, all the grains have the same values of the prefactor for different grain orientations, which means that the elastic modulus of a reference grain can be used for the computations of prefactors of all other grains.

The term e_{hom} is the elastic strain energy of a homogeneous solid solution. However, compositional distribution in a solid solution is generally inhomogeneous. The elastic strain energy stemming from the compositional inhomogeneity of the solid solution is the coherency strain energy (e_{coh}),

$$\begin{aligned} e_{\text{coh}} &= \frac{1}{2} C_{ijkl} \varepsilon_{ij}^{el} \varepsilon_{kl}^{el} \\ &= \frac{1}{2} C_{ijkl} (\bar{\varepsilon}_{ij} + \delta\varepsilon_{ij} - \varepsilon_{ij}^{\circ})(\bar{\varepsilon}_{kl} + \delta\varepsilon_{kl} - \varepsilon_{kl}^{\circ}), \end{aligned} \tag{12}$$

where ε_{ij}^{el} is the elastic strain tensor which is equal to $(\bar{\varepsilon}_{ij} + \delta\varepsilon_{ij} - \varepsilon_{ij}^{\circ})$, $\bar{\varepsilon}_{ij}$ is the homogeneous strain tensor, $\delta\varepsilon_{ij}$ is the heterogeneous strain tensor, and ε_{ij}° is the eigenstrain tensor. For an elastically anisotropic and inhomogeneous polycrystal, the position-dependent elastic modulus is modeled as the following [18,19,39]:

$$C_{ijkl}(\vec{r}) = \sum_g \eta_g^2 a_{im}^g a_{jn}^g a_{ko}^g a_{lp}^g C_{mnop}^{\text{ref}}, \tag{13}$$

where η_g is the grain order parameter, a_{ij}^g are the components of an axis transformation matrix representing the rotation from the coordinate system defined on a given grain g to the global reference coordinate system, and C_{mnop}^{ref} on the right-hand side is the elastic modulus in the coordinate system defined on the given grain and C_{mnop}^{ref} of all the grains are same.

The eigenstrain due to the compositional inhomogeneity is defined by

$$\varepsilon_{ij}^{\circ}(\vec{r}) = \varepsilon_{ij}^{m}(X(\vec{r}) - X_0), \tag{14}$$

where ε_{ij}^{m} is the misfit strain tensor, and X_0 is the overall composition of the solid solution. To represent the structural inhomogeneity of a polycrystal, we also employ the position (or grain structure)-dependent mismatch ($\varepsilon_{ij}^{m}(\vec{r})$) modeled in Equation (9).

The homogeneous strain $\bar{\varepsilon}_{ij}$ represents the macroscopic shape change of a system and is defined such that

$$\int_V \delta\varepsilon_{ij}(\vec{r}) \mathrm{d}V = 0. \tag{15}$$

When a system is constrained under a constant applied strain (ε_{ij}^{a}), the homogeneous strain is simply equal to the applied strain, i.e. $\bar{\varepsilon}_{ij} = \varepsilon_{ij}^{a}$. On the other hand,

if the boundaries are allowed to relax, the homogeneous strain in an elastically inhomogeneous polycrystal is computed by [18,19]

$$\bar{\varepsilon}_{ij} = \langle S_{ijkl}\rangle\left(\sigma^a_{kl} + \langle\sigma^0_{kl}\rangle - \langle\delta\sigma_{kl}\rangle\right), \tag{16}$$

where $\langle S_{ijkl}\rangle = \langle C_{ijkl}\rangle^{-1}$, $\langle C_{ijkl}\rangle = (1/V)\int_V C_{ijkl}(\vec{r})\mathrm{d}V$, σ^a_{ij} is an applied stress, $\langle\sigma^0_{ij}\rangle = (1/V)\int_V C_{ijkl}(\vec{r})\varepsilon^0_{kl}(\vec{r})\mathrm{d}V$, and $\langle\delta\sigma_{ij}\rangle = (1/V)\int_V C_{ijkl}(\vec{r})\delta\varepsilon_{kl}(\vec{r})\mathrm{d}V$.

The heterogeneous strain can be expressed by the elastic displacement $u_i(\vec{r})$ following Khachaturyan [2]:

$$\delta\varepsilon_{ij}(\vec{r}) = \frac{1}{2}\left(\frac{\partial u_i}{\partial r_j} + \frac{\partial u_j}{\partial r_i}\right), \tag{17}$$

To compute the heterogeneous strain field, we solve the following mechanical equilibrium equation since the mechanical equilibrium is established much faster than the diffusional processes:

$$\nabla_j\sigma_{ij} = \nabla_j\left[C_{ijkl}(\vec{r})(\bar{\varepsilon}_{kl} + \delta\varepsilon_{kl}(\vec{r}) - \varepsilon^\circ_{kl}(\vec{r}))\right] = 0, \tag{18}$$

where σ_{ij} is the local elastic stress. In order to solve the mechanical equilibrium equation with the spatially inhomogeneous elasticity in polycrystals, we employ the Fourier-spectral iterative-perturbation scheme [16,17]. To apply the method, the position-dependent elastic modulus (Equation (13)) is divided into a constant homogeneous part C^{hom}_{ijkl} (or C^{hom}_{ij}) and a position-dependent inhomogeneous perturbation part $C^{\mathrm{inhom}}_{ijkl}(\vec{r})$ (or $C^{\mathrm{inhom}}_{ij}(\vec{r})$), i.e.

$$C_{ijkl}(\vec{r}) = C^{\mathrm{hom}}_{ijkl} + \left(\sum_g \eta_g^2 a^g_{im}a^g_{jn}a^g_{ko}a^g_{lp}C^{\mathrm{ref}}_{mnop} - C^{\mathrm{hom}}_{ijkl}\right) = C^{\mathrm{hom}}_{ijkl} + C^{\mathrm{inhom}}_{ijkl}(\vec{r}), \tag{19}$$

where $C^{\mathrm{inhom}}_{ijkl}(\vec{r})$ is $(\sum_g \eta_g^2 a^g_{im}a^g_{jn}a^g_{ko}a^g_{lp}C^{\mathrm{ref}}_{mnop} - C^{\mathrm{hom}}_{ijkl})$. The details of the general procedure are discussed in [18,19]. For better efficiency, we additionally employed the Voigt notation scheme to solve the mechanical equilibrium equation. The procedure is as follows:

(1) Zeroth-order iteration: The elastic modulus is assumed to be homogeneous and solve the mechanical equilibrium equation to obtain the zeroth-order approximation of the elastic displacements. The equations in the Voigt notation are

$$\begin{aligned}
\tilde{u}^0_1 &= -i[\Omega_1(\tilde{\sigma}^0_1k_x + \tilde{\sigma}^0_6k_y + \tilde{\sigma}^0_5k_z) + \Omega_6(\tilde{\sigma}^0_6k_x + \tilde{\sigma}^0_2k_y + \tilde{\sigma}^0_4k_z)\\
&\quad + \Omega_5(\tilde{\sigma}^0_5k_x + \tilde{\sigma}^0_4k_y + \tilde{\sigma}^0_3k_z)],\\
\tilde{u}^0_2 &= -i[\Omega_6(\tilde{\sigma}^0_1k_x + \tilde{\sigma}^0_6k_y + \tilde{\sigma}^0_5k_z) + \Omega_2(\tilde{\sigma}^0_6k_x + \tilde{\sigma}^0_2k_y + \tilde{\sigma}^0_4k_z)\\
&\quad + \Omega_4(\tilde{\sigma}^0_5k_x + \tilde{\sigma}^0_4k_y + \tilde{\sigma}^0_3k_z)],\\
\tilde{u}^0_3 &= -i[\Omega_5(\tilde{\sigma}^0_1k_x + \tilde{\sigma}^0_6k_y + \tilde{\sigma}^0_5k_z) + \Omega_4(\tilde{\sigma}^0_6k_x + \tilde{\sigma}^0_2k_y + \tilde{\sigma}^0_4k_z)\\
&\quad + \Omega_3(\tilde{\sigma}^0_5k_x + \tilde{\sigma}^0_4k_y + \tilde{\sigma}^0_3k_z)],
\end{aligned} \tag{20}$$

where $\sigma^0_i = C^{\mathrm{hom}}_{ij}\varepsilon^0_j$, $\Omega^{-1}_{ik} = C^{\mathrm{hom}}_{ijkl}k_jk_l$ (Ω_{ik} is reduced to Ω_i), $i = \sqrt{-1}$, $\vec{k} = (k_x, k_y, k_z)$ is the reciprocal lattice vector, the tilde ($\sim$) represents the Fourier transform.

Downloaded by [Pennsylvania State University] at 12:08 19 July 2013

(2) Higher-order iteration: The $(n-1)$th-order elastic solution is used to obtain the nth-order elastic displacements by solving

$$\begin{aligned}
\tilde{u}_1^n &= -i[\Omega_1(\tilde{T}_1^{n-1}k_x + \tilde{T}_6^{n-1}k_y + \tilde{T}_5^{n-1}k_z) + \Omega_6(\tilde{T}_6^{n-1}k_x + \tilde{T}_2^{n-1}k_y + \tilde{T}_4^{n-1}k_z) \\
&\quad + \Omega_5(\tilde{T}_5^{n-1}k_x + \tilde{T}_4^{n-1}k_y + \tilde{T}_3^{n-1}k_z)] \\
\tilde{u}_2^n &= -i[\Omega_6(\tilde{T}_1^{n-1}k_x + \tilde{T}_6^{n-1}k_y + \tilde{T}_5^{n-1}k_z) + \Omega_2(\tilde{T}_6^{n-1}k_x + \tilde{T}_2^{n-1}k_y + \tilde{T}_4^{n-1}k_z) \\
&\quad + \Omega_4(\tilde{T}_5^{n-1}k_x + \tilde{T}_4^{n-1}k_y + \tilde{T}_3^{n-1}k_z)] \\
\tilde{u}_3^n &= -i[\Omega_5(\tilde{T}_1^{n-1}k_x + \tilde{T}_6^{n-1}k_y + \tilde{T}_5^{n-1}k_z) + \Omega_4(\tilde{T}_6^{n-1}k_x + \tilde{T}_2^{n-1}k_y + \tilde{T}_4^{n-1}k_z) \\
&\quad + \Omega_3(\tilde{T}_5^{n-1}k_x + \tilde{T}_4^{n-1}k_y + \tilde{T}_3^{n-1}k_z)],
\end{aligned} \tag{21}$$

Where $T_i^{n-1} = C_{ij}^{\text{total}}(\varepsilon_j^0 - \bar{\varepsilon}_j^{n-1}) - C_{ij}^{\text{inhom}}\delta\varepsilon_j^{n-1}$. The number of iterations is controlled by the tolerance. In this work, the iterations were continuously performed until the value of $\sqrt{\int_v[(u_1^{n+1}-u_1^n)^2+(u_2^{n+1}-u_2^n)^2+(u_3^{n+1}-u_3^n)^2]dV}$ became smaller than 1.0×10^{-4}.

Downloaded by [Pennsylvania State University] at 12:08 19 July 2013

2.2. *Strain energy contribution to thermodynamics of solid solutions*

Elastic strain energy contributions in an isotropic solid solutions were discussed in [11]. Let us consider the elastic strain energy of an elastically anisotropic solid solution in a single crystal. Ignoring the macroscopic deformation of the entire system ($\bar{\varepsilon}_{ij}=0$), the expression of coherency elastic strain energy E_{coh} of the entire system in Fourier space is given by [2]

$$E_{\text{coh}} = \frac{1}{2}\int \frac{d^3\vec{k}}{(2\pi)^3} B(\vec{n})\left|\delta\tilde{X}(\vec{k})\right|^2, \tag{22}$$

where $\vec{k}$ is the wave vector in Fourier space, $\delta\tilde{X}(\vec{k})$ is the Fourier transform of $\delta X(\vec{r}) = X - X_0$, and $B(\vec{n}) = C_{ijkl}\varepsilon_{ij}^m\varepsilon_{kl}^m - n_i\sigma_{ij}^0\Omega_{jk}\sigma_{kl}^0 n_l = C_{ijkl}\varepsilon_{ij}^m\varepsilon_{kl}^m - L(\vec{n})$. The total strain energy of the system is the sum of E_{hom} and E_{coh},

$$\begin{aligned}
E_{\text{total}}^{\text{aniso}} &= E_{\text{hom}} + E_{\text{coh}} \\
&= \frac{1}{2}\int_V [C_{ijkl}\varepsilon_{ij}^m\varepsilon_{kl}^m - \langle L(\vec{n})\rangle_{\vec{n}}]X(1-X)\mathrm{d}V \\
&\quad + \frac{1}{2}\int \frac{d^3k}{(2\pi)^3}\left[C_{ijkl}\varepsilon_{ij}^m\varepsilon_{kl}^m - L(\vec{n})\right]\left|\delta\tilde{X}(\vec{k})\right|^2.
\end{aligned} \tag{23}$$

The second term in Equation (23) can be split into two parts:

$$\begin{aligned}
\frac{1}{2}\int \frac{d^3k}{(2\pi)^3}\left[C_{ijkl}\varepsilon_{ij}^m\varepsilon_{kl}^m - L(\vec{n})\right]\left|\delta\tilde{X}(\vec{k})\right|^2 &= \frac{1}{2}\int \frac{d^3k}{(2\pi)^3}\left[C_{ijkl}\varepsilon_{ij}^m\varepsilon_{kl}^m - \langle L(\vec{n})\rangle_{\vec{n}}\right]\left|\delta\tilde{X}(\vec{k})\right|^2 \\
&\quad + \frac{1}{2}\int \frac{d^3k}{(2\pi)^3}\left[\langle L(\vec{n})\rangle_{\vec{n}} - L(\vec{n})\right]\left|\delta\tilde{X}(\vec{k})\right|^2,
\end{aligned} \tag{24}$$

where the first term of the right-hand side is the orientation-independent part and the second term of the right-hand side is the orientation-dependent part of the coherency

strain energy. Applying the Parseval's theorem to the orientation-independent part and adding to e_{hom}, it produces the following:

$$\begin{aligned}
&\frac{1}{2}\int_V \left[C_{ijkl}\varepsilon_{ij}^m\varepsilon_{kl}^m - \langle L(\vec{n})\rangle_{\vec{n}}\right]X(1-X)\mathrm{d}V + \frac{1}{2}\int \frac{d^3k}{(2\pi)^3}\left[C_{ijkl}\varepsilon_{ij}^m\varepsilon_{kl}^m - \langle L(\vec{n})\rangle_{\vec{n}}\right]\left|\delta\tilde{X}(\vec{k})\right|^2 \\
&\quad = \frac{1}{2}\int_V \left[C_{ijkl}\varepsilon_{ij}^m\varepsilon_{kl}^m - \langle L(\vec{n})\rangle_{\vec{n}}\right]X(1-X)\mathrm{d}V + \frac{1}{2}\int_V \left[C_{ijkl}\varepsilon_{ij}^m\varepsilon_{kl}^m - \langle L(\vec{n})\rangle_{\vec{n}}\right](X-X_0)^2\mathrm{d}V \\
&\quad = \frac{1}{2}V\left[C_{ijkl}\varepsilon_{ij}^m\varepsilon_{kl}^m - \langle L(\vec{n})\rangle_{\vec{n}}\right]X_0(1-X_0).
\end{aligned} \tag{25}$$

Thus, the total elastic strain energy of the elastically anisotropic system can be written as

$$\begin{aligned}
E_{\text{total}}^{\text{aniso}} &= \frac{1}{2}V\left[C_{ijkl}\varepsilon_{ij}^m\varepsilon_{kl}^m - \langle L(\vec{n})\rangle_{\vec{n}}\right]X_0(1-X_0) \\
&\quad + \frac{1}{2}\int \frac{d^3k}{(2\pi)^3}\left[\langle L(\vec{n})\rangle_{\vec{n}} - L(\vec{n})\right]\left|\delta\tilde{X}(\vec{k})\right|^2.
\end{aligned} \tag{26}$$

which is consistent with Khachaturyan's expression of the elastic strain energy of a solid solution [2]. For an elastically isotropic solution, the second term of Equation (26) becomes zero since $L(\vec{n})$ is equal to $\langle L(\vec{n})\rangle_{\vec{n}}$ and the first term reduces to

$$\begin{aligned}
&2\mu\left(\frac{1+\nu}{1-\nu}\right)\varepsilon_c^2 X_0(1-X_0) \quad \text{(in three dimensions)} \\
&\text{or} \quad \left(\frac{\mu}{1-\nu}\right)\varepsilon_c^2 X_0(1-X_0), \quad \text{(in two dimensions)}
\end{aligned} \tag{27}$$

where μ is the shear modulus and ν is the Poisson's ratio. This means that the elastic strain energy of elastically isotropic solid solution is not affected by the compositional distribution (Crum theorem). Based on the above discussion, we could confirm that both e_{hom} and e_{coh} are essential components for the elastic strain energy of a solid solution.

The elastic strain energy significantly contributes to the thermodynamics of spinodal boundaries. As Khachaturyan discussed in [2], only the orientation-dependent part of the coherency strain energy affects the coherent spinodal boundaries with respect to the chemical spinodal boundaries since the homogeneous part of free energy should include the orientation-independent part of coherency strain energy. Our model correctly describes the spinodal boundary. The local free energy density can be expressed as

$$f = \left(f_{\text{chem}} + e_{\text{hom}} + e_{\text{coh}}^{\text{indep}}\right) + e_{\text{coh}}^{\text{dep}}. \tag{28}$$

The second derivative of $(e_{\text{hom}} + e_{\text{coh}}^{\text{indep}})$ is equal to zero, i.e.

$$\frac{\partial^2}{\partial X^2}\left(\frac{1}{2}\left[C_{ijkl}\varepsilon_{ij}^m\varepsilon_{kl}^m - \langle L(\vec{n})\rangle_{\vec{n}}\right]X(1-X) + \frac{1}{2}\left[C_{ijkl}\varepsilon_{ij}^m\varepsilon_{kl}^m - \langle L(\vec{n})\rangle_{\vec{n}}\right](X-X_0)^2\right) = 0. \tag{29}$$

Downloaded by [Pennsylvania State University] at 12:08 19 July 2013

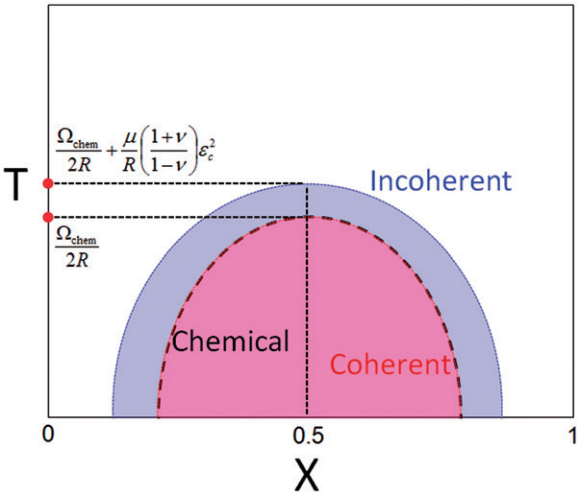

Figure 2. (colour online) Schematic diagram of the spinodal regimes.

Therefore, the difference in spinodal regimes between chemical spinodal and coherent spinodal is also determined by the only second derivative of $(f_{\text{chem}} + e_{\text{coh}}^{\text{dep}})$, while the incoherent spinodal regime is determined by the second derivative of $(f_{\text{chem}} + e_{\text{hom}})$, which is the incoherent free energy. In the case of an isotropic elastic solid solution, the coherent spinodal boundaries are the same as chemical spinodal since $e_{\text{coh}}^{\text{dep}}$ becomes zero, and the incoherent spinodal regime is wider than coherent or chemical spinodal regimes. Moreover, the consolute temperature of the incoherent spinodal decomposition is higher than that of chemical or coherent spinodal decomposition by $\frac{\mu}{R}(\frac{1+\nu}{1-\nu})\varepsilon_c^2$. A schematic illustration of the spinodal regime is shown in Figure 2 Thus, we could conclude that the elastic strain energy terms defined in our model correctly describe the diffusional processes.

2.3. *Diffusion kinetics*

The temporal evolution of the compositional fields X is governed by the Cahn–Hilliard equation [43]:

$$\frac{\partial X(\vec{r},t)}{\partial t} = \nabla \cdot M_c \nabla\left(\frac{\delta F}{\delta X(\vec{r},t)}\right), \tag{30}$$

where M_c is the interdiffusion mobility, and $\left(\frac{\delta F}{\delta X}\right)$ is the variational derivative of the free energy functional with respect to composition. Substituting the total free energy F (Equation (1)) with the expressions in Equation (8) into Equation (30), we obtain the following kinetic equations:

$$\frac{\partial X}{\partial t} = \nabla \cdot M_c \nabla\left(\frac{\partial f_{\text{chem}}}{\partial X} - m\omega g + \frac{\partial e_{\text{hom}}}{\partial X} + \frac{\partial e_{\text{coh}}}{\partial X} - \kappa_c \nabla^2 X\right), \tag{31}$$

Downloaded by [Pennsylvania State University] at 12:08 19 July 2013

The derivatives of e_{hom} and e_{coh} with respect to X in Equation (31) are derived using Equations (11) and (12):

$$\begin{aligned}\frac{\partial e_{\text{hom}}}{\partial X} &= \frac{1}{2}\left[C_{ijkl}\varepsilon_{ij}^{m,b}\varepsilon_{kl}^{m,b} - \langle L^b(\vec{n})\rangle_{\vec{n}}\right]\varphi(\vec{r})^2(1-2X),\\ \frac{\partial e_{\text{coh}}}{\partial X} &= -C_{ijkl}(\bar{\varepsilon}_{ij} + \delta\varepsilon_{ij} - \varepsilon_{ij}^{\circ})\left(\frac{\partial \varepsilon_{kl}^{\circ}}{\partial X}\right) = -C_{ijkl}\varepsilon_{ij}^{el}\varepsilon_c\delta_{kl}\varphi(\vec{r}),\end{aligned} \tag{32}$$

We employed the variable interdiffusion mobility for M_{c} in Equation (30) which is given by

$$M_c = M_c^0 X(1-X), \tag{33}$$

where M_c^0 is the prefactor which is equal to D/RT, D is the interdiffusion coefficient, R is the gas constant, and T is the temperature. To solve the Cahn–Hilliard equation with the composition-dependent diffusion mobility, the numerical technique for the variable mobility in [44] is employed. The Cahn–Hilliard equation (Equation (30)) is solved by the semi-implicit Fourier-spectral method [44,45].

Downloaded by [Pennsylvania State University] at 12:08 19 July 2013

3. Simulation results and discussions

3.1. *Preparation of grain structures and numerical input parameters*

Even though the model is applicable to simultaneous grain growth and compositional evolutions, we will mainly discuss compositional evolution on a static grain structure for simplicity. To generate grain structures described by multiple grain order parameters, we employ the following local free energy density functional for $g(\eta_1, \eta_2, \ldots, \eta_g)$ in Equation (1) based on the model in [46] in the present model:

$$g(\eta_1, \eta_2, \ldots, \eta_g) = 0.25 + \sum_g \left(-\frac{1}{2}\eta_g^2 + \frac{1}{4}\eta_g^4\right) + \gamma \sum_g \sum_{g'>g} \eta_g^2\eta_{g'}^2, \tag{34}$$

where γ is the phenomenological parameter for the interactions among grain order parameters. A constant 0.25 in Equation (34) is employed to make the value of the function g equal to 0 inside the bulk to describe zero interaction potential ($-m\omega g$ in Equation (7)) inside the grain for convenience, which does not affect the kinetics of the grain structure evolution. The evolution of the non-conserved order parameters η_{g} is governed by the Allen–Cahn relaxation equation [47]:

$$\frac{\partial \eta_g(\vec{r}, t)}{\partial t} = -L\left(\frac{\delta F}{\delta \eta_g(\vec{r}, t)}\right), \tag{35}$$

where L is the kinetic coefficient related to grain boundary mobility, t is time, and $(\frac{\delta F}{\delta \eta_g})$ is the variation of the free energy function with respect to the grain order parameter fields. The equations are solved by semi-implicit Fourier-spectral method [45].

The kinetic equations in Equations (31) and (35) were solved in dimensionless forms. The parameters were normalized by $\Delta x^* = \frac{\Delta x}{l}$, $\Delta t^* = LE\Delta t$, $\omega^* = \frac{\omega}{E}$, $\mu^* = \frac{\mu}{E}$, $f^* = \frac{f}{E}$, $C_{ij}^* = \frac{C_{ij}}{E}$, $\kappa^* = \frac{\kappa}{El^2}$, and $M_c^{0*} = \frac{M_c^0}{Ll^2}$ where E is the characteristic energy which was chosen to be $10^9\,\text{J/m}^3$ and l is the characteristic length which is taken

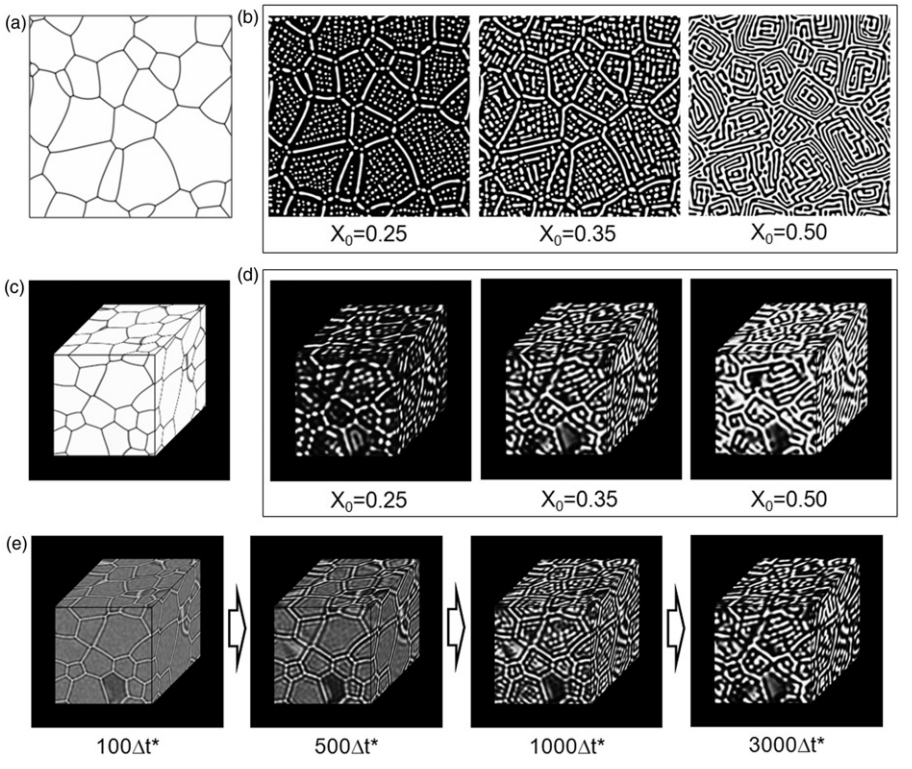

Figure 3. Examples of phase-field simulations. (a) Two-dimesional (2D) grain structure, (b) diffusional process in the 2D grain structure with diverse overall compositions, (c) three-dimensional (3D) grain structure, (d) diffusional process in the 3D grain structure with diverse overall compositions, and (e) the temporal evolution of a composition in the 3D grain structure when $X_0 = 0.35$.

to be 2×10^{-9} m. For a reference grain, we used the elastic constants of γ phase in Ni–Al alloy system used in [31] which were estimated from [48,49]. The normalized elastic constants in Voigt notation were $C_{11}^{ref^*} = 195.8$, $C_{12}^{ref^*} = 144.0$, and $C_{44}^{ref^*} = 89.6$. Each grain in a polycrystal is elastically anisotropic since the Zener anisotropy factor A_Z $(= 2C_{44}^{ref^*}/(C_{11}^{ref^*} - C_{12}^{ref^*}))$ is equal to 3.46. The composition expansion coefficient ε_c is chosen to be 0.04. The dimensionless gradient energy coefficients κ_c^* and κ_o^* are set to be 0.25. The interaction parameter m was taken to be 0.5, and the normalized height ω^* was chosen to be 1.14. The terms associated with the normalized chemical free energy such as μ°^*}, $\mu_h^{\circ^*}$, and Ω_{chem}^* were set to be 1.0, 1.0, and 2.0, respectively. The prefactor $M_c^{0^*}$ of interdiffusion mobility in dimensionless unit in Equation (33) was chosen as 0.118. The dimensionless grid size Δx^* was 0.5, and time step Δt^* for integration was 0.1. All the simulations were conducted with the periodic boundary condition.

Examples of generated grain structures in two (2D) and three dimensions (3D) are shown in Figure 3a and c. For these random grain structures, circular (2D) or spherical (3D) grains were randomly distributed in the system at the initial stage and the system was relaxed by solving Equation (35). Once the grain structure is

Downloaded by [Pennsylvania State University] at 12:08 19 July 2013

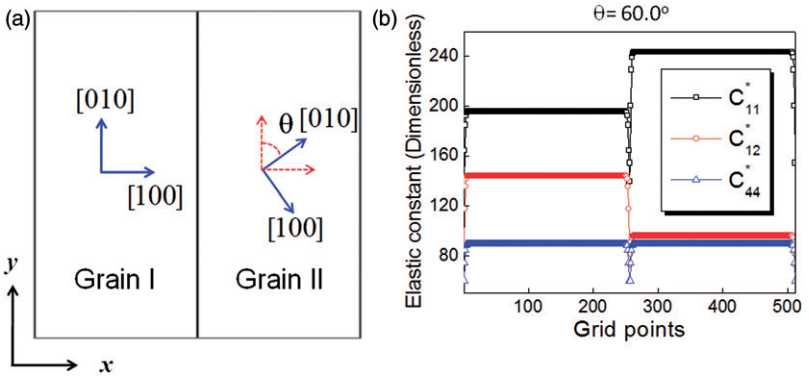

Figure 4. (colour online) (a) Simulation setup in a bicrystal generated by a phase-field simulation, and (b) profiles of elastic constants (C^*_{11}, C^*_{12}, C^*_{44}) with respect to (x–y) coordinate system across a grain boundary when $\theta = 60^\circ$.

prepared, the local free energy density g in Equation (7) is computed and fixed for the composition–grain structure interaction term ($-m\omega gX$). On the prepared static grain structures, we perform the computer simulations of the diffusion processes taking into account the chemical and elastic interactions between solute and grain boundaries. Some examples of the simulations with different overall compositions are shown in Figure 3b for 2D and Figure 3d for 3D. To nucleate the precipitates, the Gaussian random fluctuations were incorporated to the compositional field at the early stage. Figure 3e shows the temporal evolution of compositional field in a 3D grain structure, and the solute–grain boundary interaction, i.e. grain boundary segregation, is clearly shown at the early stage of the simulation.

3.2. *Precipitate–precipitate interaction across a grain boundary*

The elastic stress field generated by a coherent precipitate in one grain may influence the precipitations in other grains since the elastic interactions are long-range. To investigate the interactions between precipitates in different grains, we designed a simple bicrystal as shown in Figure 4a. We labeled the left-hand side grain as Grain I and the right-hand side grain as Grain II. We can vary the misorientation between two adjoining grains as well as the locations of precipitates inside the grains. As an example, the grain orientation of Grain I is fixed as 0°, while Grain II is oriented at an angle of 60° with respect to Grain I. The distributions of the elastic constants (C^*_{11}, C^*_{12}, and C^*_{44}) with respect to the global reference coordinate system (x-y frame) are plotted across a grain boundary in Figure 4b.

The elastic stress field generated by a coherent precipitate in an elastically anisotropic solid is strongly orientation-dependent. Figure 5a shows contour plots of the computed spatial distributions of the elastic stress fields ($\sigma_{xx}, \sigma_{xy}, \sigma_{yy}$) generated from a single coherent precipitate in a bicrystal. For comparison, the stress fields in a single crystal are also plotted in Figure 5b. In both cases, the stress fields from the precipitate propagate over a long range. However, as one can clearly see, the stress

Downloaded by [Pennsylvania State University] at 12:08 19 July 2013

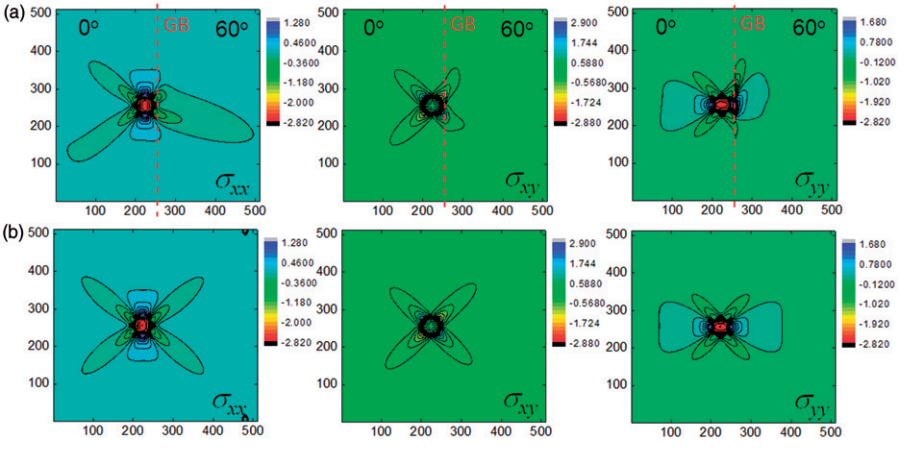

Figure 5. (colour online) Contour plots of elastic stress fields ($\sigma_{xx}, \sigma_{xy}, \sigma_{yy}$) generated from a single coherent precipitate (a) in a bicrystal (red dashed line represents a grain boundary) and (b) a single crystal.

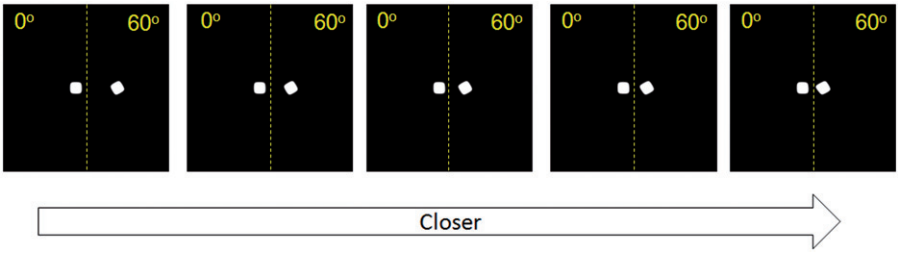

Figure 6. (colour online) Morphology of precipitates in a bicrystal. A precipitate in Grain I is located at a fixed position, while a precipitate in Grain II is placed at several different distances to a grain boundary. A yellow dashed line represents the location of a grain boundary.

fields, especially, σ_{xx} and σ_{yy}, abruptly change across the grain boundary. It means that precipitates in Grain II might be affected by the distorted elastic stress fields, and the effects would be more significant if the precipitates are located near the grain boundary.

To observe the precipitation reaction under the stress fields near a grain boundary, we initially introduced two circular precipitates of $R = 20\Delta x^*$ and monitor the temporal evolution of the precipitate morphology. One was embedded in Grain I at a fixed location, while the other was embedded in Grain II at several different distances to the grain boundary, as shown in Figure 6, to observe the influence of the different levels of stress field on the precipitate. To reduce the overlap of the elastic field due to the periodic boundary condition, we employ a relatively large system ($512\Delta x^* \times 512\Delta x^*$ grids). The solute composition in the matrix was taken to be 0.046, which is close to one of the equilibrium compositions ($X_{\mathrm{eq}}^{\mathrm{matrix}} = 0.037$ and $X_{\mathrm{eq}}^{\mathrm{precipitate}} = 0.963$).

Downloaded by [Pennsylvania State University] at 12:08 19 July 2013

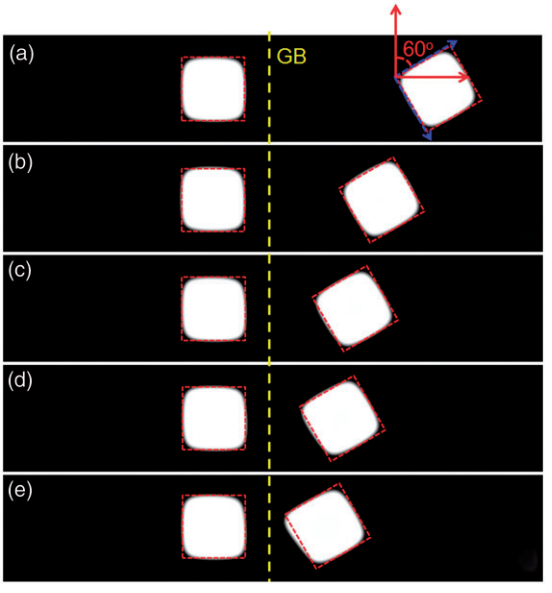

Figure 7. (colour online) Morphology of precipitates near a grain boundary for the cases in Figure 6 (zoomed images of Figure 6). The yellow dashed line represents the location of a grain boundary.

Figure 7 shows the zoomed images of Figure 6 in order to clearly capture the morphology of precipitates near the grain boundary for several precipitate locations in Grain II. First of all, the morphology of the precipitate is cubic with rounded corners, as shown in Figure 7a. The precipitate embedded in Grain II is rotated by 60° with respect to the precipitate embedded in Grain I. The precipitates in the configuration of Figure 7a do not seem to significantly affect each other. As the precipitate in Grain II becomes closer to the grain boundary (see Figure 7b–e), the interesting features are captured. The morphology of the precipitate in Grain II deviates from the perfect cuboidal shape (see Figure 7e). This means that the diffusion process associated with the precipitate in Grain II is interfered by a bias.

Diffusion kinetics is generally affected by the elastic stress field. The relationship between the diffusion flux and the elastic stress field is given by [1]:

$$J = cM(F - X_i \Delta\Omega \nabla P), \tag{36}$$

where J is the flux, c is the total concentration, M is the diffusion mobility, F is the driving force for diffusion except the local pressure effect, X_i is the mole fraction of species i, $\Delta\Omega$ is the pure dilation during the atomic jump, and P is the local pressure defined by $[-(\sigma_{xx} + \sigma_{yy})/2]$ in two dimensions and $[-(\sigma_{xx} + \sigma_{yy} + \sigma_{zz})/3]$ in three dimensions. For convenience, we use the negative local pressure $(-P = (\sigma_{xx} + \sigma_{yy})/2)$. By the definition, the positive value of $-P$ represents the tensile local pressure and the negative value represents the compressive local pressure. Consequently, the diffusion kinetics can be significantly affected by the local pressure fields. Thus, we investigated the local pressure distribution near precipitates in order

Downloaded by [Pennsylvania State University] at 12:08 19 July 2013

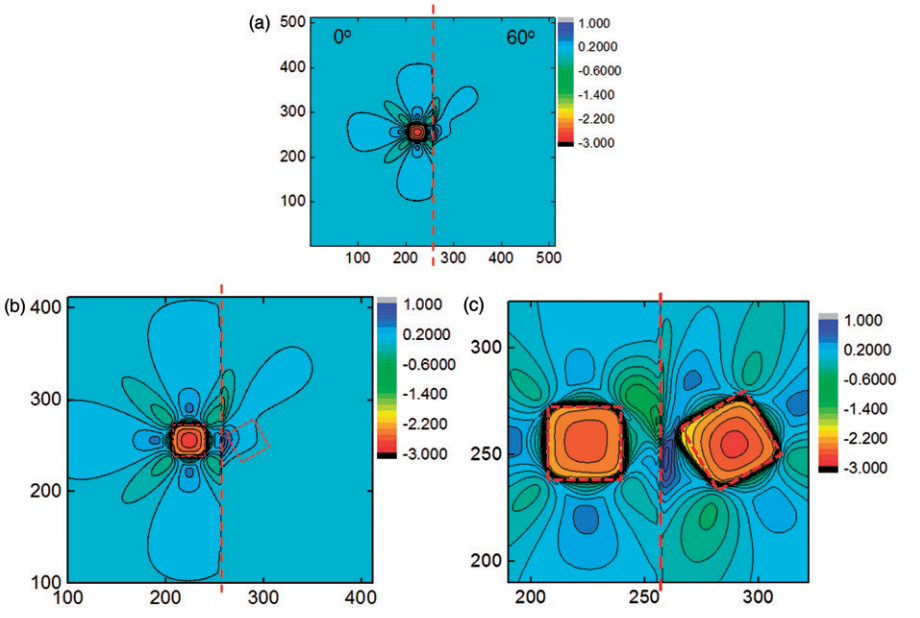

Figure 8. (colour online) (a) Contour plot of negative local pressure ($-P$) generated from a single coherent precipitate in Grain I in a bicrystal, (b) magnified plot of $-P$ with the guidelines of the precipitates in Figure 7e, and (c) contour plot of $-P$ generated from two coherent precipitates in Grain I and II with the guidelines of the precipitates in Figure 7e.

to explore the origin of the deformed shape of the precipitate. Figure 8a shows contour plot of $-P$ $(= (\sigma_{xx} + \sigma_{yy})/2)$ distribution which arises due to a single coherent precipitate in Grain I. In the external area of the precipitate, the local pressure along the diagonal direction of the precipitate is more compressive. On the other hand, the local pressure along the normal direction to a flat interface of the precipitate is more tensile. The local pressure field elongates to the grain boundary, and it is refracted when it passes though the grain boundary in the same way as the stress fields. As a result, the irregular tensile regime next to the grain boundary is formed in Grain II. In Figure 8b, the guidelines of the coherent precipitates of Figure 7e, where the precipitate in Grain II is closest to the grain boundary, are shown in the enlarged contour plot in order to observe the effect of the local pressure. Most deviation of the morphology (from the perfect cuboidal shape) occurs near the tensile region, i.e. the left hand side corner of the precipitate in Grain II tends to be dragged toward the more tensile regime. Figure 8c shows the distribution of $-P$ when the other coherent precipitate is also placed at Grain II. Even though the local pressure field displays the more distorted distribution due to the superposition of local pressure fields from both coherent precipitates, it clearly shows the distortion of the precipitate shape in Grain II toward the tensile regime. It should be mentioned that the shape of the precipitate in Grain I is also distorted since the local pressure distribution around the precipitate in Grain I is influenced by the stress field

Downloaded by [Pennsylvania State University] at 12:08 19 July 2013

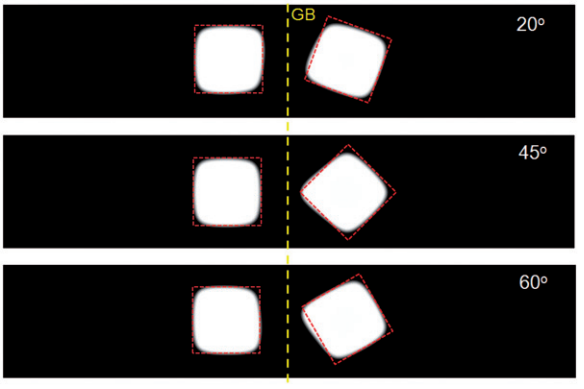

Figure 9. (colour online) Morphology of precipitates near a grain boundary for the cases of different crystallographic orientations of Grain II. The yellow dashed line represents the location of a grain boundary.

Downloaded by [Pennsylvania State University] at 12:08 19 July 2013

generated from the precipitate in Grain II, which results in strongly asymmetric local pressure distribution near the precipitate in Grain I.

We also conducted simulations with different crystallographic orientations of Grain II, and similar behavior is observed, as shown in Figure 9. Morphological shapes of two precipitates are mutually influenced by each other. This can be one of reasons for the irregular morphology of precipitates near or at grain boundaries which have significantly important implications to the mechanical properties.

3.3. *Precipitate–grain boundary segregation interaction*

The effects of elastic strain energy on grain boundary segregation profiles have been discussed in [11] for the case of isotropic elastic modulus. In this section, we discuss the effects of elastic stress generated by the precipitates within grains on solute segregation at grain boundaries in elastically anisotropic systems.

It is easily expected that the elastic stress field or local pressure profile along a grain boundary stemming from the multiple coherent precipitates in adjacent grains is strongly inhomogeneous. In addition, it would depend on the spatial configuration of the precipitates. Figure 10b shows the negative local pressure ($-P$) profiles along the grain boundary (shaded region in Figure 10a) in the cases of different grain orientations of Grain II. Corresponding solute composition profiles along the grain boundary are shown in Figure 10c. In all cases, the solute composition at the locally maximum compressive region (shaded in red) is relatively low, while the composition at the relatively tensile (locally minimum compressive) regions (shaded in blue) tends to be at local maximum. The solute atoms do not prefer compressive stress regions since the solute lattice parameter expansion coefficient is dilatational and positive. As a result, the composition profile along the grain boundary is non-uniform depending on the configurations of coherent precipitates inside grains. Similar behaviors of solute segregation/depletion near a dislocation were discussed in [50].

Downloaded by [Pennsylvania State University] at 12:08 19 July 2013

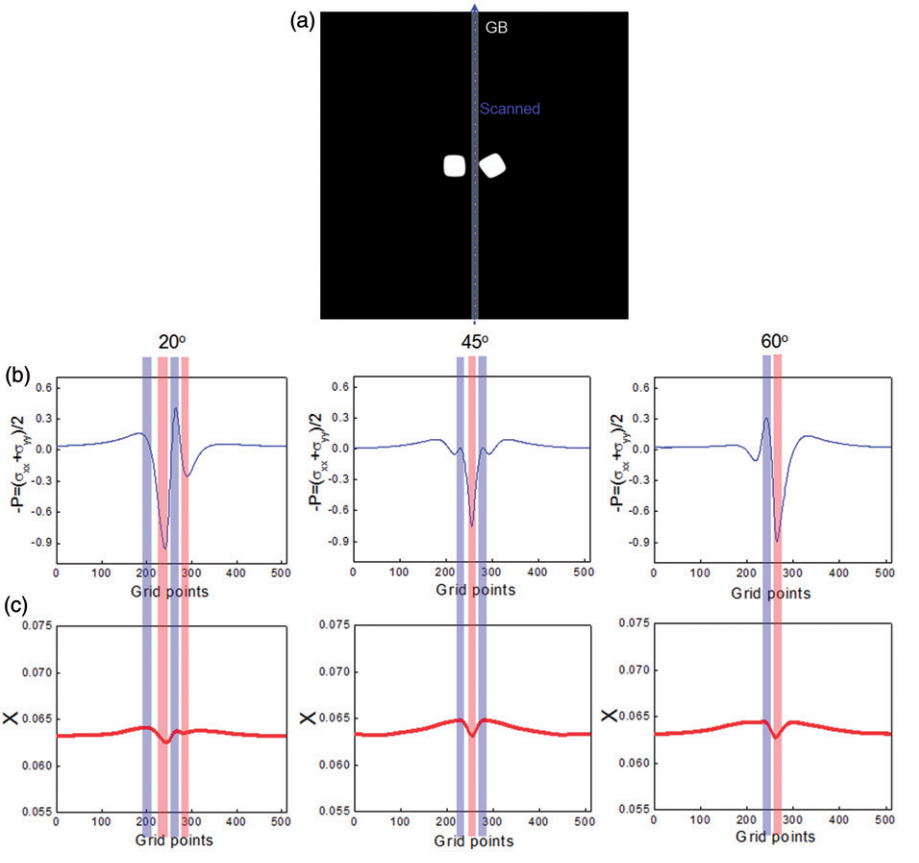

Figure 10. (colour online) (a) Scanned regime for the profiles of negative local pressure ($-P$) and solute composition. (b) Negative local pressure ($-P$) profiles along the grain boundary in the cases of different grain orientations of Grain II, and (c) corresponding solute composition profiles along the grain boundary.

Finally, the non-uniform distribution of solute atoms at a grain boundary can supply the inhomogeneous distribution of candidate sites for secondary (barrier-less) nucleation at the grain boundary. We performed the simulations at higher matrix composition ($X_m = 0.12$), i.e. a supersaturated system, in the presence of primary coherent precipitates inside grains. We monitored the secondary nucleation process at a grain boundary. Figure 11a shows the temporal evolution of the process. New precipitates are nucleated along the grain boundary region within dashed line in the figure. Depending on the spatial configuration of primary coherent precipitates, the secondary nucleation events along the grain boundary occur at different locations, as shown in Figure 11b. For better comparison, the composition profiles along the grain boundary are plotted in Figure 11c. The figure clearly shows the non-uniform distribution of the secondary nucleation. This phenomenon can happen in realistic materials systems. For instance, upon the continuous cooling, the nucleation of the secondary γ' precipitates occurs in the presence of the pre-existing primary coherent

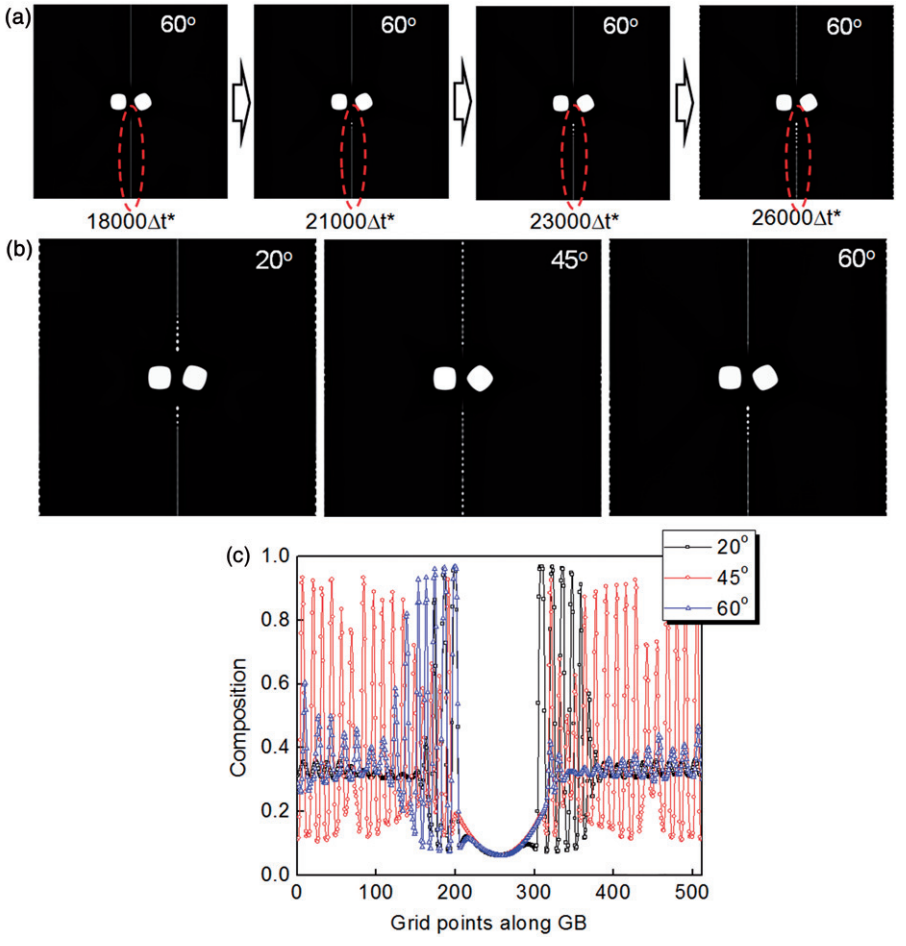

Figure 11. (colour online) (a) Snapshots of the secondary nucleation process of precipitates at a grain boundary. (b) Secondary nucleation of precipitates at a grain boundary with different grain orientations of Grain II, and (c) composition profiles along the grain boundary.

γ' phase in Ni alloys, which results in the bimodal distribution of γ' precipitates [51]. Our simulation results indicate that the primary γ' precipitates inside grains can affect the spatial distribution of grain boundary nucleated secondary γ' precipitates. In addition, the grain boundary precipitate distribution may affect mechanical behavior, e.g. creep rate [52].

4. Summary

We have incorporated the elastic strain energy contribution in the phase-field model of grain boundary segregation in an elastically anisotropic polycrystalline solid solution. The elastic strain energy of a solid solution was obtained by solving the

Downloaded by [Pennsylvania State University] at 12:08 19 July 2013

mechanical equilibrium equation using the iterative-perturbation Fourier spectral method. We investigated the elastic interactions between precipitates in different grains, and between precipitates and grain boundary segregation. The elastic stress fields from a coherent precipitate inside grain propagate across a grain boundary which may affect the shape of precipitates in other grains near the grain boundary. Precipitates near a grain boundary generate non-uniform stress field or local pressure along a grain boundary, leading to inhomogeneous grain boundary segregation which in turn may induce non-uniform nucleation of secondary precipitates along a grain boundary. We are currently applying this model to a number of polycrystalline materials systems involving the diffusional processes, such as Ti alloys, Ni alloys, Zr alloys, etc.

Downloaded by [Pennsylvania State University] at 12:08 19 July 2013

Acknowledgements

This work was funded by the Center for Computational Materials Design (CCMD), a joint National Science Foundation (NSF) Industry/University Cooperative Research Center at Penn State (IIP-1034965) and Georgia Tech (IIP-1034968), and computer simulations were carried out on the CyberSTAR cluster funded by NSF through Grant OCI-0821527.

References

[1] R.W. Balluffi, S.M. Allen and W.C. Carter, *Kinetics of Materials*, John Wiley and Sons, New Jersey, 2005.
[2] A.G. Khachaturyan, *Theory of Structural Transformations in Solids*, John Wiley and Sons, New York, 1983.
[3] M. Doi, Progr. Mater. Sci. 40 (1996) p.79.
[4] P. Fratzl, O. Penrose and J. Lebowitz, J. Stat. Phys. 95 (1999) p.1429.
[5] Y.U. Wang, Y.M. Jin and A.G. Khachaturyan, J. Appl. Phys. 91 (2002) p.6435.
[6] D. Fan, S.P. Chen and L.-Q. Chen, J. Mater. Res. 14 (1999) p.1113.
[7] P.-R. Cha, S.G. Kim, D.-H. Yeon and J.-K. Yoon, Acta Mater. 50 (2002) p.3817.
[8] K. Grönhagen and J. Ågren, Acta Mater. 55 (2007) p.955.
[9] S.G. Kim and Y.B. Park, Acta Mater. 56 (2008) p.3739.
[10] J. Li, J. Wang and G. Yang, Acta Mater. 57 (2009) p.2108.
[11] T.W. Heo, S. Bhattacharyya and L.-Q. Chen, Acta Mater. 59 (2011) p.7800.
[12] Y.U. Wang, Y.M. Jin and A.G. Khachaturyan, J. Appl. Phys. 92 (2002) p.1351.
[13] M. Tonks, P. Millett, W. Cai and D. Wolf, Scripta Mater. 63 (2010) p.1049.
[14] D.-U. Kim, S.G. Kim, W.T. Kim, J. Cho, H.N. Han and P.-R. Cha, Scripta Mater. 64 (2011) p.1079.
[15] D.-U. Kim, P.-R. Cha, S.G. Kim, W.T. Kim, J. Cho, H.-N. Han, H.-J. Lee and J. Kim, Comput. Mater. Sci. 56 (2012) p.58.
[16] S.Y. Hu and L.-Q. Chen, Acta Mater. 49 (2001) p.1879.
[17] P. Yu, S.Y. Hu, L.-Q. Chen and Q. Du, J. Comput. Phys. 208 (2005) p.34.
[18] S. Bhattacharyya, T.W. Heo, K. Chang and L.-Q. Chen, Model. Simulat. Mater. Sci. Eng. 19 (2011) p.035002.
[19] S. Bhattacharyya, T.W. Heo, K. Chang and L.-Q. Chen, Comm. Comput. Phys. 11 (2012) p.726.
[20] L.-Q. Chen, Annu. Rev. Mater. Res. 32 (2001) p.113.

[21] W.J. Boettinger, J.A. Warren, C. Beckermann and A. Karma, Annu. Rev. Mater. Res. 32 (2002) p.163.
[22] L. Granasy, T. Pusztai, T. Börzsönyi, G. Toth, G. Tegze, J.A. Warren and J.F. Douglas, J. Mater. Res. 21 (2006) p.309.
[23] H. Emmerich, Adv. Phys. 57 (2008) p.1.
[24] N. Moelans, B. Blanpain and P. Wollants, Comput. Coupling Phase Diagr. Thermochem. 32 (2008) p.268.
[25] I. Steinbach, Model. Simulat. Mater. Sci. Eng. 17 (2009) p.073001.
[26] Y.M. Jin, A. Artemev and A.G. Khachaturyan, Acta Mater. 49 (2001) p.2309.
[27] A. Artemev, Y. Jin and A.G. Khachaturyan, Phil. Mag. A 82 (2002) p.1249.
[28] Y.U. Wang, Y. Jin and A.G. Khachaturyan, Acta Mater. 52 (2004) p.1039.
[29] S. Choudhury, Y.L. Li, C.E. Krill III and L.-Q. Chen, Acta Mater. 53 (2005) p.5313.
[30] S. Choudhury, Y.L. Li, C. Krill III and L.-Q. Chen, Acta Mater. 55 (2007) p.1415.
[31] J.Z. Zhu, Z.-K. Liu, V. Vaithyanathan and L.-Q. Chen, Scripta Mater. 46 (2002) p.401.
[32] J.Z. Zhu, T. Wang, A.J. Ardell, S.H. Zhou, Z.-K. Liu and L.-Q. Chen, Acta Mater. 52 (2004) p.2837.
[33] T. Wang, G. Sheng, Z.-K. Liu and L.-Q. Chen, Acta Mater. 56 (2008) p.5544.
[34] D.Y. Li and L.-Q. Chen, Acta Mater. 46 (1998) p.2573.
[35] V. Vaithyanathan, C. Wolverton and L.-Q. Chen, Phys. Rev. Lett. 88 (2002) 125503.
[36] V. Vaithyanathan, C. Wolverton and L.-Q. Chen, Acta Mater. 52 (2004) p.2973.
[37] H. Ramanarayan and T.A. Abinandanan, Acta Mater. 51 (2003) p.4761.
[38] H. Ramanarayan and T.A. Abinandanan, Acta Mater. 52 (2004) p.921.
[39] T.W. Heo, S. Bhattacharyya and L.-Q. Chen, Solid State Phenom. 172–174 (2011) p.1084.
[40] J.W. Cahn, J. Chem. Phys. 28 (1958) p.258.
[41] J.W. Cahn, Acta Metall. 10 (1962) p.789.
[42] J.W. Cahn, *The Mechanisms of Phase Transformations in Crystalline Solids*, Sidney Press, Bedford, 1968, p.1.
[43] J.W. Cahn, Acta Metall. 9 (1961) p.795.
[44] J. Zhu, L.-Q. Chen, J. Shen and V. Tikare, Phys. Rev. E 60 (1999) p.3564.
[45] L.-Q. Chen and J. Shen, Comput. Phys. Comm. 108 (1998) p.147.
[46] L.-Q. Chen and W. Yang, Phys. Rev. B 50 (1994) p.15752.
[47] S.M. Allen and J.W. Cahn, Acta Metall. 27 (1979) p.1085.
[48] S.V. Prikhodko, J.D. Carnes, D.G. Isaak and A.J. Ardell, Scripta Mater. 38 (1998) p.67.
[49] S.V. Prikhodko, J.D. Carnes, D.G. Isaak, H. Yang and A.J. Ardell, Metall. Mater. Trans. A 30 (1999) p.2403.
[50] S.Y. Hu and L.-Q. Chen, Acta Mater. 49 (2001) p.463.
[51] Y.H. Wen, J.P. Simmons, C. Shen, C. Woodward and Y. Wang, Acta Mater. 51 (2003) p.1123.
[52] X.-J. Wu and A.K. Koul, Metall. Mater. Trans. A 26 (1995) p.905.

Downloaded by [Pennsylvania State University] at 12:08 19 July 2013

Appendix. Calculation of $\langle L(\vec{n})\rangle_{\vec{n}}$

By definition, $\langle L(\vec{n})\rangle_{\vec{n}}$ is the average of $L(\vec{n})$ over all the directions of $\vec{n}$ where $L(\vec{n}) = n_i\sigma^0_{ij}\Omega_{jk}\sigma^0_{kl}n_l$, $\sigma^0_{ij} = C_{ijkl}\varepsilon^m_{kl}$, $\Omega^{-1}_{jk} = C_{jilk}n_in_l$, and n_i is the unit wave vector in Fourier space. The mathematical expression of $\langle L(\vec{n})\rangle_{\vec{n}}$ is given by [2]

$$\langle L(\vec{n})\rangle_{\vec{n}} = \frac{1}{4\pi}\oint L(\vec{n})\mathrm{d}\Omega, \tag{A1}$$

where $d\Omega$ is the solid angle element. Since $\frac{1}{(\frac{4\pi}{3}r_k^3)}\int_0^{r_k} 4\pi k^2 dk = 1$, Equation (A1) becomes

$$\langle L(\vec{n})\rangle_{\vec{n}} = \frac{1}{\left(\frac{4\pi}{3}r_k^3\right)}\int_0^{r_k} 4\pi k^2 dk \cdot \frac{1}{4\pi}\oint L(\vec{n})d\Omega, \tag{A2}$$

where r_k is an arbitrary radius of a sphere in k-space. Applying the definition of the solid angle ($d\Omega = \sin\theta d\theta d\phi$), we obtain

$$\langle L(\vec{n})\rangle_{\vec{n}} = \frac{1}{\left(\frac{4\pi}{3}r_k^3\right)}\int_0^{2\pi}\int_0^{\pi}\int_0^{r_k} L(\vec{n})k^2 \sin\theta dk d\theta d\phi = \frac{1}{\left(\frac{4\pi}{3}r_k^3\right)}\int\int\int_{\substack{\text{sphere}\\ r=r_k}} L(\vec{n})d^3k. \tag{A3}$$

Therefore, $\langle L(\vec{n})\rangle_{\vec{n}}$ becomes the spherical average. In [2], the Debye cutoff radius (k_d) defined by the relation $\frac{4\pi}{3}k_d^3 = \frac{(2\pi)^3}{v_0}$ where $\frac{(2\pi)^3}{v_0}$ is the volume of the first Brillouin zone was chosen for the radius of the sphere, and $\langle L(\vec{n})\rangle_{\vec{n}}$ was calculated by

$$\langle L(\vec{n})\rangle_{\vec{n}} = \frac{1}{\left(\frac{4\pi}{3}k_d^3\right)}\int\int\int_{\substack{\text{sphere}\\ r=k_d}} L(\vec{n})d^3k = \frac{1}{\left[\frac{(2\pi)^3}{v_0}\right]}\int\int\int_{\substack{\text{sphere}\\ r=k_d}} L(n)d^3k. \tag{A4}$$

It should be noted that we can also take any r_k within the first Brillouin zone. Thus, we can take the integration over the sphere whose radius is equal to $\pi/\Delta x$ for the spherical average. Hence, $\langle L(\vec{n})\rangle_{\vec{n}}$ can be computed as

$$\langle L(\vec{n})\rangle_{\vec{n}} = \frac{1}{\left(\frac{4\pi}{3}\left(\frac{\pi}{\Delta x}\right)^3\right)}\int\int\int_{\substack{\text{sphere}\\ r=\pi/\Delta x}} L(\vec{n})d^3k = \frac{1}{V_k}\int\int\int_{\substack{\text{sphere}\\ r=\pi/\Delta x}} L(n)d^3k. \tag{A5}$$

in the numerical calculations where V_k represents the volume of sphere whose radius is equal to $\pi/\Delta x$.

Downloaded by [Pennsylvania State University] at 12:08 19 July 2013